Publisher homepage: www.universepg.com, ISSN: 2707-4625 (Online) & 2707-4617 (Print)
https://doi.org/10.34104/ijmms.020.071086
International Journal of Material and Mathematical Sciences
Journal homepage: www.universepg.com/journal/ijmms

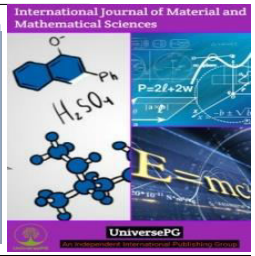

Synthesis, Characterization and Pressure Effect on Structural and Mechanical Properties of $MgBi_2O_6$: Solid-State Route and DFT Study

Md. Atikur Rahman[1]*, Md. Afjalur Rahman[2], and Abdur Razzaque Sarker[3]

[1,2]Department of Physics, Pabna University of Science and Technology, Pabna-6600, Bangladesh; and [3]Department of Physics, Rajshahi University, Rajshahi-6205, Bangladesh.

*Correspondence: atik0707phy@gmail.com (Md. Atikur Rahman, Assistant Professor, Department of Physics, Pabna University of Science and Technology, Pabna, Bangladesh).

ABSTRACT

Here we have prepared good quality crystalline sample $MgBi_2O_6$ employing the solid state reaction technique. The synthesized material was characterized by XRD and SEM (scanning electron microscopy). The structural study confirmed that $MgBi_2O_6$ possesses tetragonal crystal configuration (JCPDS PDF#, No. 86-2492) with outstanding crystallinity and a grain size between 200 to 350 nm. The temperature dependence electrical resistivity and conductivity were measured by two probe methods and ensured the semiconducting nature of this material. Using the impedance analyzer and UV-visible spectrophotometer we studied the experimental electronic and optical properties of this material. To explore the hypothetical features of $MgBi_2O_6$ we have used first principles methods which depend on CASTEP code. The band structure analysis also ensured the semiconducting nature of $MgBi_2O_6$ with small band gap of 0.12 eV. The semiconducting behavior of $MgBi_2O_6$ with band gap of 0.12 eV was also observed by the band structure analysis. The Born's stability criteria were fulfilled by the investigated elastic constants and ensured the stable nature of $MgBi_2O_6$. The response of structural and mechanical properties with pressure of $MgBi_2O_6$ was discussed in details. We have also studied the hypothetical optical properties of $MgBi_2O_6$ by CASTEP code.

Keywords: Solid-state reaction, First-principles routes, TGA, SEM, FTIR analysis, and Optical properties.

1. INTRODUCTION:

Nowadays, semiconductor photocatalysis has attarcted a lot of attention in view of the fact that it offers a profitable and environmentally secure option for pollution purification, high efficiency, energy saving and conversion (Zou *et al*., 2011; Kudo and Miseki, 2009; Chen *et al*., 2010; Linic *et al*., 2011). Fujishima and Honda, (1972) was first reported about the photocatalytic activity of TiO_2 which is one of the most popular photocatalysts, has been broadly studied due to its nontoxicity, outstanding oxidative power, high stability, low cost and photostability (Tang *et al*., 2007; Matsuda and Hatano, 2005). Unfortunately, due to the wide band gap of about 3.2 eV, TiO_2 is only active in the UV region which only involves in about 4% of the incident solar radiation. Therefore, it is severely limits the efficient usage of solar energy. Moreover, TiO_2 reveals low quantum efficiency due to the high recombination rate of photo-induced electron-hole pairs (Long *et al*., 2006; Jiang and Wang, 2007). Hence, in order to make full utilize of sunlight it is urgently essential to discover more efficient materials with visible-light-driven photocatalytic activity. In present years, numerous bismuth-based semi-conductors have received extraordinary attention due to their high photocatalytic activity (Meng and Zhang, 2016). In these compounds, bismuth normally presents in trivalent

or pentavalent states. Recently, some Bi^{3+} containing materials for example $BiVO_4$ (Kudo *et al.*, 1999), Bi_2WO_6 (Fu *et al.*, 2005), and BiOCl (Wang *et al.*, 2017) have been broadly explored as new candidates for visible-light-responsive photo-catalysts due to the exceptional electronic configuration essentially arising from the hybridization of O-2p and filled Bi-6s orbitals. Additionally, the empty 6s orbital of Bi^{5+} also leads to some Bi^{5+} including compounds having tremendous photo-catalytic activity. Alternatively, a number of Bi oxides having remarkable pentavalent state ($Bi^{5+)}$ have received a lot of attention for their research interest. Among these bismuth oxides a famous example is $NaBiO_3$ which show as a strong absorber of visible light and has significant application in photo-oxidation of organic materials (Kako *et al.*, 2007).

Recently Gong *et al.* (2017) proposed that the compound $AgBiO_3$ has the ability to create large quantity of reactive oxygen species with no light illumination and has an exceptional oxidizing activity. The compound $BaBiO_3$ having both Bi^{3+} and Bi^{5+} states, can be used as a potential absorber of all-oxide photovoltaic (Chouhan *et al.*, 2018) and show photocatalyst behavior in the case of visible-light irradiation (Liu *et al.*, 2019). With trirutile structure the compound $MgBi_2O_6$ shows outstanding photo-catalytic manners for methylene blue degradation (Takei *et al.*, 2011). This compound was first synthesized by Kumada *et al.* (2003) employing the hydrothermal method. In 2003, Mizoguchi *et al.* (2011) investigated the electrical and optical features of $MgBi_2O_6$ and mentioned that it is a degenerate n-type semiconductor with relatively narrow band gap of about 1.8 eV. Having special band configuration, the compound $MgBi_2O_6$ can be used as visible light-sensitive photocatalysts for disintegration of carbonic species. The theoretically investigated band gap of $MgBi_2O_6$ is found to be1.10 eV carried out by Heyd-Scuseria-Ernzerhof (HSE) functional method (Zhang *et al.*, 2018).

In this work we have investi-gated the detailed physical properties of $MgBi_2O_6$ by first-principles method with GGA and PBE and have seen that this phase shows metallic behavior (Rahman *et al.*, 2016). The characteristic has also been found by Lin Liu, Dianhui Wang *et al.* in 2019. Therefore to obtain the band gap of this compound they have used HSE functional scheme instead of GGA, PBE route. But fortunately in our present work we have successfully observed the band gap of $MgBi_2O_6$ by using the GGA and PBE route. In this work, we have also synthesized the high quality $MgBi_2O_6$ crystals via the solid-state reaction method and characterized the as-prepared sample by XRD, SEM, impedance analyzer and UV-visible spectrophotometer. Furthermore, using first-principles method we have calculated the structural and mechanical properties of this compound under different pressures for the first time.

2. METHODOLOGY:

2.1 Experimental methodology - In this research work, the pure $MgBi_2O_6$ crystal was produced through the usual solid-state reaction method with the high purity (purity > 98 %) powders of MgO and Bi_2O_5. In order to begin the synthesizing process of $MgBi_2O_6$, initially we have studied the phase development of this phase using a thermobalance (TG/DTA 630). A stoichiometric mixture of MgO and Bi_2O_5 was heated in an air atmosphere through a heating program as shown in the inset of **Fig 1**. A characteristics TG curve attained from the mixture of raw materials (MgO and Bi_2O_5) is also revealed in **Fig 1**.

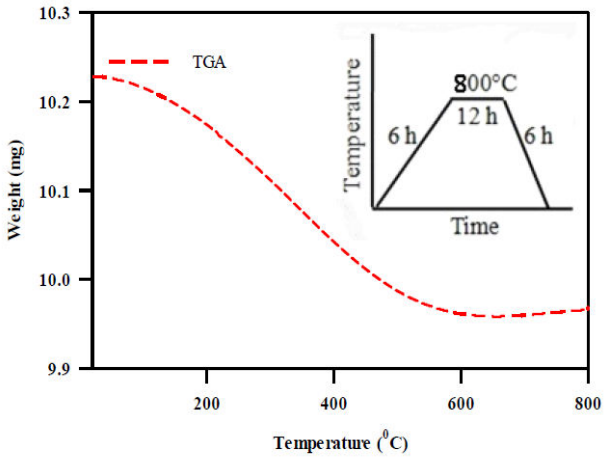

Fig 1: Thermogravimetric (TGA) curve (with heat program) for phase formation process of $MgBi_2O_6$.

From this TG curve, it was noticed that the weight loss at 100-580°C is too large. This result confirm that at temperature lower than 100°C, the chemical reaction between the raw materials may not be active so far and there is no weight change above 600°C where the phase formation is done. At the primary step of synthesis, the reactants were dried in air an oven at 100 °C for 12 h. The powder mixture of MgO and Bi_2O_5 was mixed well in an agate mortar with ethanol then dried and calcined at 800 °C for 12

h at ambient. Before the next heat treatment the mixture was grounded again to ensure homogeneity. The powder was calcined second time at 850 °C for 12 h at atmosphere. After the second heat conduct, the powder was grounded and pelletized in 12 mm diameter under the pressure of 80 KN by using pressure gauze. At atmosphere the pellet was sintered at 900°C for 12 h. During the heat treatment process the raising- cooling rates of temperature were fixed to 3 °C/min. The powder sample of $MgBi_2O_6$ was analyzed by using the X-ray powder diffraction spectroscopy with CuK_α (λ = 0.15418 nm) radiation source at room temperature in Centre for Advanced Research in Sciences (CARS), in Bangladesh. The sample was scanned at the diffraction angle (2θ) within the range of 5° and 85°. The structural and morphological investigation of the prepared sample was carried out by scanning electron microscopy (SCM). For investigating the FTIR spectrum of the powder sample, we have used Fourier transform infrared (FTIR) spectrophotometer (Spectrum 100, Perkin Elmer). The Agilent Precision impedance analyzer (Agilent technologies, Model 4294A Japan) was used for the measurement of frequency-dependent ac conductance, impedance, dielectric constant, capacitance, inductance and reactance.

2.2 Theoretical methodology - The detailed physical properties of magnesium bismuth oxide, $MgBi_2O_6$ has been carried out through the CASTEP computer code (Clark *et al.*, 2005) within the frame of density-functional theory (DFT). By employing the Perdew-Burke-Ernzerhof (PBE) method (Perdew *et al.*, 1996) we have treated the exchange-correlation energy within the generalized gradient approximation (GGA). For pseudo atomic computations, Mg-$2p^6$ $3s^2$, Bi- $6s^2$ $6p^3$ and O- $2s^2$ $2p^4$ have been taken as the valence electron states. The plane wave basis set with cut-off energy 480 eV is employed to expand the wave functions. For sampling the Brillouin zone a Monkhorst-Pack grid of 10×10×5 k-points was used for compound $MgBi_2O_6$. In order to obtain the equilibrium crystal structure of $MgBi_2O_6$ the Broyden-Fletcher-Goldfarb- Shanno (BFGS) minimization scheme was used. The succeeding criteria for the geometry optimization were sited to 5.0×10^{-5} eV/atom for total energy, 0.01 eV/Å for maximum force, 0.02 GPa for maximum stress and 5.0×10^{-4} Å for maximum atomic displacement. The stress-strain system was used to find out the single independent elastic constants of $MgBi_2O_6$ (Kang *et al.*, 2003; Mostari *et al.*, 2020). We have used the Voigt-Reuss-Hill approximations to compute the poly-crystalline elastic constants of $MgBi_2O_6$.

3. RESULTS AND DISCUSSION:

3.1. Experimental and Theoretical Structural Properties - The structural analysis of $MgBi_2O_6$ has performed by X-ray diffractometer (XRD) (Rigaku Ultima IV X-Ray Diffractometer) with CuKα radiation (λ = 0.15418 nm) from 10º-80º, with a scan speed of 5º/min. The unit cell refinement has been performed by Cell Call program employing the XRD data. The X-ray diffraction pattern of $MgBi_2O_6$ is displayed in **Fig 2** which ensured the single phase tetragonal crystal structure of this material with space group of $P4_2/mnm$ (No. 136) and lattice parameters a = b = 4.841, c = 9.721 Å (JCPDS PDF#, No. 86-2492) (Kumada *et al.*, 1997). The experimental, theoretically investigated lattice parameters and atomic co-ordinates of $MgBi_2O_6$ are listed in **Table 1**. From **Table 1**, we have seen that our experimental lattice parameters are approximately equal to the standard lattice parameters obtained from the stated JCPDS data and satisfied the previous work. The optimized lattice parameters are very close to our experimental data which insured the reliability of the DFT based simulation. The sharp and strong diffraction peaks (**Fig 2**) reveals the excellent crystallinity of $MgBi_2O_6$. The larger value of inten-sity ratio reveals the better crystallinity (Hu *et al.*, 2007). Here, the intensity ratio of the highest peaks (110) and second highest peak (103) is 2.21 which is large than the critical value 1.2 (Hao *et al.*, 2005) and confirms the better crystallinity of $MgBi_2O_6$. The higher crystallinity would promote to yield higher photocatalytic activity (Zhong *et al.*, 2018).

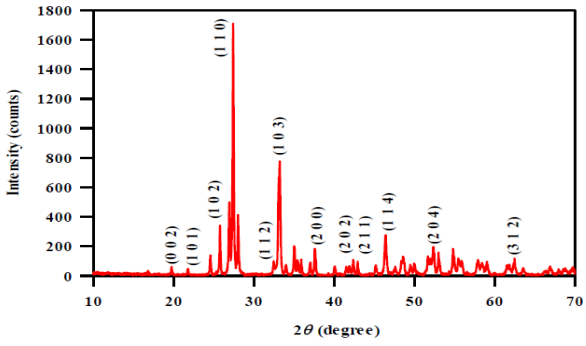

Fig 2: X-ray diffraction patterns of $MgBi_2O_6$.

To study the effect of external pressure on the crystal structure of $MgBi_2O_6$, we have studied the variations of the lattice parameters, unit cell

volume and bulk modulus of $MgBi_2O_6$ with different pressures up to 50 GPa. For this investigation we have used generalized gradient approximation depend on DFT based calculations implement in CASTEP code. The variations of the cell volume, lattice parameters and bulk modulus of $MgBi_2O_6$ with pressure are presented in **Fig 3**. From **Fig 3** we have seen that the lattice parameters and the cell volume of $MgBi_2O_6$ are decrease with increases of pressure, consequently the bulk modulus, B_0 increased with the increase of pressure. However, the atomic distance is reduced with increasing pressure. For this reason, the repulsive attraction between atoms becomes string, which guides to the complexity of compression of the material under pressure (Rahman *et al.*, 2016). The lattice parameters, cell volume and bulk modulus with different pressures are listed in **Table 2**.

Table 1: Lattice parameters and atomic positions of $MgBi_2O_6$.

Lattice parameters (Å), unit cell-volume (Å^3), and axial angles (degree)	**Atoms**	**Position type**	**x**	**y**	**z**	**Ref.**
a = b = 4.841*, c = 9.721*, V = 227.81*, α = γ = β = 90°* [*Expt. Work]	Mg	2a	0	0	0	This work
	Bi	4e	0	0	0.331	
a = b = 4.936, c = 9.832, V = 239.55, α =γ = β = 90° [Theoretical work at 0 pressure]	O1	4f	0.304	0.304	0	
	O2	8j	0.308	0.308	0.334	
a = b = 4.826*, c = 9.719*, V = 226.36*, α = γ = β = 90°*	Mg	2a	0	0	0	Kumada *et al.*, 1997
	Bi	4e	0	0	0.332	
	O1	4f	0.305	0.305	0	
	O2	8j	0.307	0.307	0.335	

Table 2: Lattice parameters *a*, *c* (Å), cell volume, *V* (Å^3) and bulk modulus, B_0 (GPa) under different pressures of $MgBi_2O_6$.

Pressure (GPa)	**Lattice parameters**		**Cell volume, *V***	**Bulk modulus, B_0**
	a	*c*		
0	4.936	9.832	239.55	130.87
10	4.794	9.703	223.07	328.99
20	4.694	9.606	211.75	531.73
30	4.621	9.516	203.19	667.17
40	4.553	9.450	195.96	750.83
50	4.493	9.397	189.74	891.27

FT-IR Analysis - The FTIR analysis is an investigative scheme which offers elementary information about the chemical bonding and phase formation of materials, whether organic or inorganic (Fairooz and Imran, 2013). This analysis also provides the information about the vibration frequency of efficient groups, network configurations of sample and cation situation in oxides (Amdouni *et al.*, 2003: Khatun *et al.*, 2014). The FTIR absorption spectrum of crystalline sample $MgBi_2O_6$ in the range of 225-4000 cm^{-1} is displayed in **Fig 4**. All spectra are typically distributed in two wave number ranges 400-950 cm^{-1} in the far-infrared region and 1000-2000 cm^{-1} in the infrared region. The main absorption bands are observed at 468.70, 677.01, 844.82, 1101.35, 1395.53, 1475.54, 1624.06, 1717.65, 2854.65, 2922.16, 3435.22, 3689.88 and 3774.69 cm^{-1}. These results verify the XRD examinations viewing that the vibration bands for precursors vanished and the vibration bands for the oxide network are built up. In the far-infrared region, we have seen a single well-resolved band at 468.70 cm^{-1} in $MgBi_2O_6$ due to an asymmetric stretching motion of MgO_6 octahedron which is distorted enormously (Kim *et al.*, 2012: Julien *et al.*, 2004). It is the unique finger of Mg site occupancy in the $MgBi_2O_6$ crystal arrangement. The absorption bonds at 677.01 and 844.82 cm^{-1} are attributed due to the symmetric and asymmetric stretching of BiO_5 units, respectively (Tang *et al.*, 2013). The sharp absorption bands at 1101.35 cm^{-1} in $MgBi_2O_6$ are consigned to Bi = O stretching mode (Song *et al.*, 2009). The absorption bands in the region of 500-800 cm^{-1} are due to the

asymmetric or sym-metric stretching of Bi-O-Bi bonds (Gao *et al.*, 1994). Furthermore the bands at around 420 cm^{-1} can be assigned to the stretching modes of Mg-O. A sharp medium absorption peak at 1624.65 cm^{-1} is found because of the stretching (vibrations) of magnesium bismuth crystal lattice. Two weak peaks are also detected at 2854.56 and 2922.16 cm^{-1} that was related to O-H bond stretching into the sample. The structural deformation is mainly shown by the existence of new broad band's at 1395.53, and 3435.22 cm^{-1} (Janjua *et al.*, 2014).

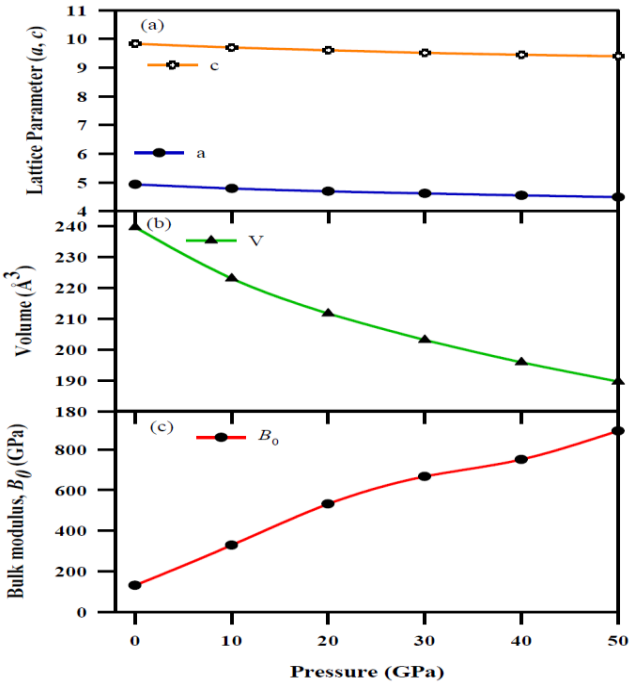

Fig 3: (a) Variations of lattice parameters, (b) cell volume, and (c) bulk modulus of $MgBi_2O_6$ with different pressure.

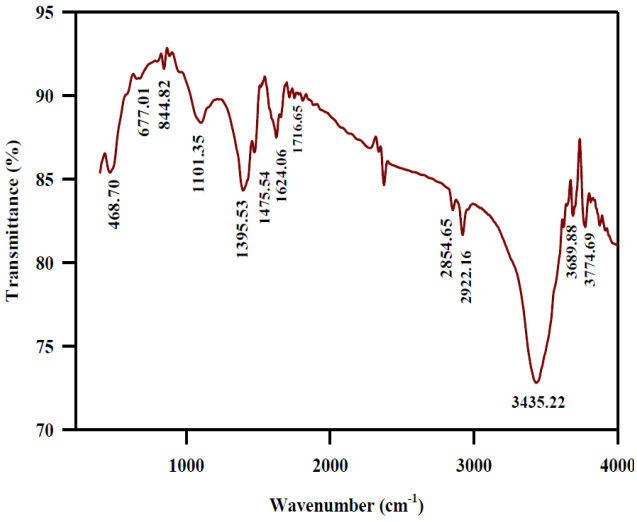

Fig 4: FT-IR spectrum of sample $MgBi_2O_6$.

SEM Analysis - The morphology and microstructure of the as-prepared pure sample $MgBi_2O_6$ was measured by scanning electron microscopy (SEM) at different magnifications as shown in **Fig 5**. From **Fig 5**, it can be seen that the photocatalyst material $MgBi_2O_6$ was composed of cuboid-like particles with the grain size of about 200 to 350 nm. In **Fig 5(c)**, $MgBi_2O_6$ particles show better crystallinity and closer arrangement and look more regular and compact (Zhong *et al.*, 2018). The higher crystallinity would promote to yield higher photocatalytic activity, since the recombination of photogenerated electron-hole pairs can be suppressed in the highly crystalline photocatalysts (Hudo *et al.*, 1999).

3.2. Experimental Electronic Properties - Using the two probe methods from room temperature to 600 K, we have measured the electrical resistivity and dc conductivity of $MgBi_2O_6$ which are shown in **Fig 6** (**a**, and **b**). From **Fig 6(a)**, we have seen that the values of resistivity of compound $MgBi_2O_6$ are decreased with increasing the temperature. For this reasons the conductivity of this material is increased with increasing temperature as shown in **Fig 6(b)**.

This analysis ensured the semiconducting manner of this material. Our results coincide with the previous study of $MgBi_2O_6$ (Takei *et al.*, 2011). Impedance spectroscopy is relatively a new and powerful routine of analyzing many of the electrical features of electrolyte materials and their interfaces. The frequency dependent dielectric constant, conductance, resistance, capacitance, reactance and impedance of $MgBi_2O_6$ are displayed in **Fig 7** which was measured within the range 100 Hz to 2 MHz at ambient temperature with the oscillating voltage 500 mV. For this measurement silver paste was coated on both surface of the sample $MgBi_2O_6$. From the dielectric property analysis, we have seen that the value of the dielectric constant of $MgBi_2O_6$ is measured to 0.75 at 100 Hz which ensure the semiconducting nature of this phase. This characteristic is also observed from the resistivity analysis shown in **Fig 6(a)**.

In the high frequency region the dielectric constant is decreased because the dipoles are not capable to rotate rapidly with the increase of frequency. For this reason their oscillations begin to lag behind to the applied field. As the frequency is further increased, the dipole will be totally unable to follow the field and the orientation polarization will be stopped (Sarkar *et al.*, 2016).

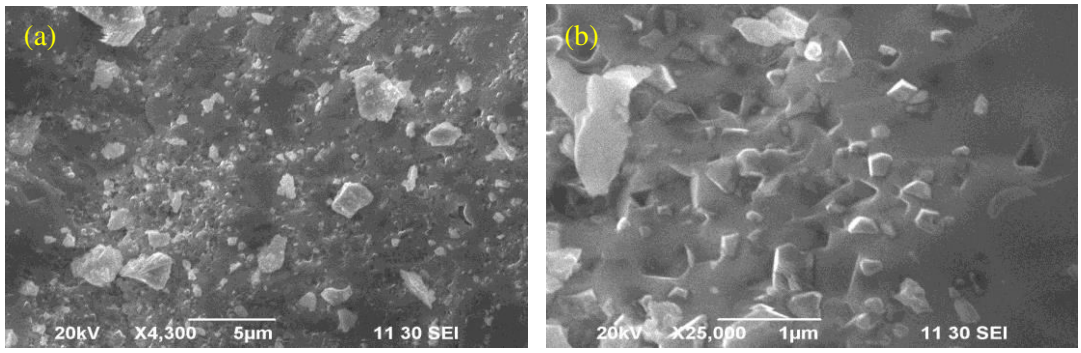

Fig 5: SEM images of $MgBi_2O_6$ at different magnifications.

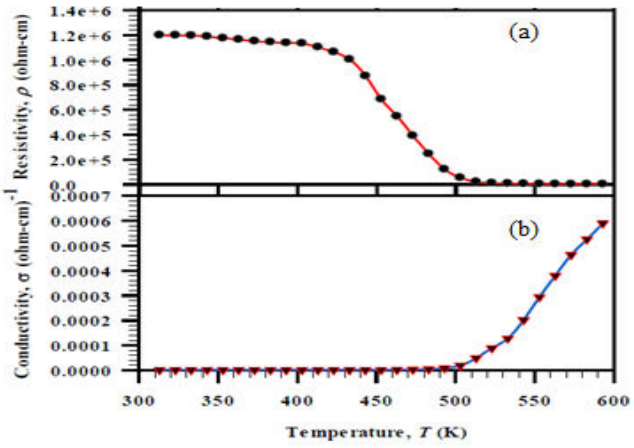

Fig 6: The temperature dependent electrical (a) resistivity and (b) conductivity of $MgBi_2O_6$.

The frequency-dependent ac conductance of the synthesized sample $MgBi_2O_6$ was measured by precision impedance analyzer within the frequency range 100 Hz to 2MHz with applied oscillating voltage of 500 mV. From **Fig 7(b)** we have seen that the conductance is increased rapidly with the increase of frequency. The mobile charge carriers contribute to this conductivity. Following the ion-hopping rules, the ionic conduction of $MgBi_2O_6$ is created from the transfer of exchangeable channels and cavities of the grains. The mobile charge carriers face some displacement between the two minimum potential energy states when they jump to a new site from its original position. This is due to the polarization of dipoles (Usha *et al.*, 2007). The maximum conductance is observed at the high frequency (~2 MHz). **Fig 7(c)** represents the frequency dependent resistance of $MgBi_2O_6$ measured with oscillating voltage 500 mV. At 100 Hz the value of the resistance of $MgBi_2O_6$ is approximately 3236.65 MΩ. Due to semiconducting manner the value of the resistance decreases with the increase of frequency in the low frequency region and approaching a constant value at above 0.08 MHz.

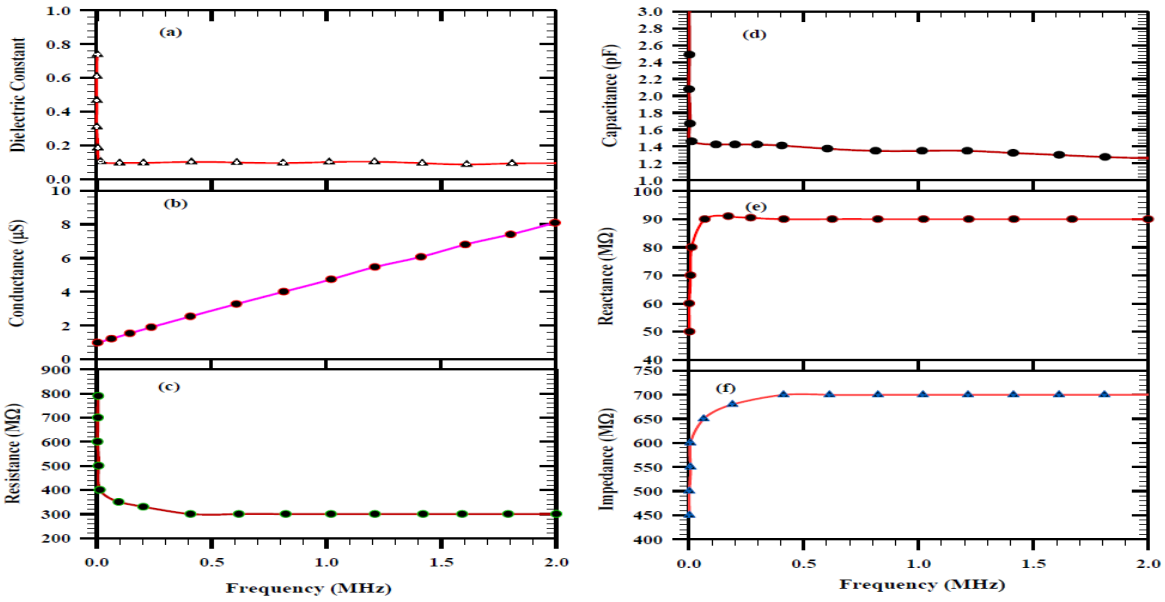

Fig 7: Frequency dependent (a) Dielectric constant, (b), Conductance, (c) Resistance, (d) Capacitance, (e) Reactance and (f) Impedance of $MgBi_2O_6$ material.

The frequency dependent capacitance of $MgBi_2O_6$ is shown in **Fig 7(d)** measured at 500 mV with a precision impedance analyzer. The high value of capacitance is observed in the low frequency region (**Fig 7d**) which is due to the due to the involvement of all kinds of polarizations at low frequency region. The capacitance is decreased with the increase of frequency and come close to almost constant value at above 1.0 MHz. This is due to the change of space charge, ionic and orientation polarizations at higher frequencies. **Fig 7(e)** and **(f)** represent the frequency dependent reactance and impedance of $MgBi_2O_6$ sample respectively within 100 Hz to 2 MHz. All these parameters are high in the low frequency region and gradually decrease in the high frequency region. The reactance is almost independent of frequency at higher frequencies (above 0.4 MHz) which is due the resistance effect.

3.3. Experimental Optical Properties - The analysis of optical function of material is very crucial due to the fact that it has some vital applications in optical coatings, reflectors, absorbers and various optoelectronic devices. The reported results on optical absorption and transmission of $MgBi_2O_6$ crystals are not available in literature. In this study, the UV–visible absorption spectrum and the transmittance of $MgBi_2O_6$ crystal were recorded using a UV-visible spectrophotometer (Shimazu: UV-1650 PC) within the photon wavelength 200 to 800 nm.

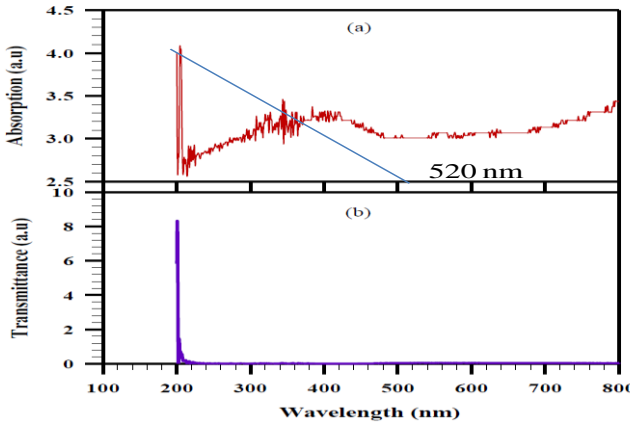

Fig 8: The wavelength dependent (a) absorption spectrum, and (b) transmittance of $MgBi_2O_6$.

Fig 8 (**a**, and **b**) illustrate the absorption spectra and transmittance of compound $MgBi_2O_6$. From **Fig 8(a)** we have seen two absorption peaks in the ultraviolet region which ensures the absorption criteria of this material in this region. No absorption peaks are found in the visible site. However the absorption increases and the transmittance decreases with the increase of wavelength in the visible region. The optical band gap energy can be calculated by using the following equation -

$$E_g = \frac{hc}{\lambda}$$

Where 'E_g' is the optical band gap, 'h' is the Plank's constant, 'c' is the velocity of light and λ is the wavelength at the edge of the absorption peak.

Here, $\lambda = 522 \times 10^{-9}$ m

Therefore, $E_g = \frac{6.626\times10^{-34}\times2.99\times10^{8}}{520\times10^{-9}}$ joule

Or, $E_g = \frac{3.8\times10^{-19}}{1.6\times10^{-19}}$ eV

Therefore, $E_g = 2.39$ eV

This band gap indicates that the sample is a semiconductor material. This feature has also found from the dielectric and resistivity analysis. The same results ensured the reliability of our present work.

3.4 Theoretical Mechanical Properties - Elastic constants are incredibly exceptional parameter of any crystalline material. These constants provide a relation between the mechanical features and dynamic information regarding the nature of the forces working in solids, particularly for the stability and hardness of materials (Wang and Zhou, 2004). The elastic constants provide fundamental information about solid-state phenomenon for example rigidity, fragility, ductile feature, anisotropy and stability behavior of a material. So it is very essential to study the stiffness constants of a material and also essential to know how the elastic feature varies with different pressures. The elastic constants of $MgBi_2O_6$ are calculated from a linear fit of the stress-strain function as said by Hook's law. Since our synthesized material is belong to tetra-gonal crystal system, it has six independent elastic constants which are listed in **Table 3**. We are unable to compare our results due to absence of experimental measurement of elastic constants data in literature. However our investigated results are in well accord with the previous theoretical work (Liu *et al.*, 2019). There some slide variation in our investigated results from the previous study which is due to the use of different calculation methods.

Table 3 also included the elastic constants of $MgBi_2O_6$ at different pressures which are totally new investigation about this material. For mechanical stability the single independent elastic constants of a tetragonal system should convince the recognized Born stability criteria which are as follows:

$$\left.\begin{array}{l} C_{11} > 0,\ C_{44} > 0,\ C_{33} > 0,\ C_{66} > 0 \\ C_{11} + C_{33} - 2C_{13} > 0,\ C_{11} - C_{12} > 0 \\ 2(C_{11} + C_{12}) + C_{33} + 4C_{13} > 0 \end{array}\right\} \quad (1)$$

From **Table 3** we have observed that the investigated independent elastic constants of our synthesized compound are positive and fulfill the above stability conditions which demonstrating that $MgBi_2O_6$ is mechanical stable in nature. From **Table 3** we have observed that C_{33} is higher than C_{11} signifying that the chemical bonding strength in the (001) direction is considerably stronger than bonding strength in the (100) and (010) directions. Additionally, C_{44} is clearly smaller than C_{66} indicating that it is very easy to occurs shear deformation in (001) direction than (010) direction (Liu *et al.*, 2019).

Table 3: The calculated elastic constants C_{ij} (in GPa) of $MgBi_2O_6$ at different pressures.

Compounds	Pressure (GPa)	C_{11}	C_{12}	C_{13}	C_{33}	C_{44}	C_{66}	Ref.
$MgBi_2O_6$	0	147.60	87.90	84.70	278.90	65.10	131.50	This work
		171.80	110.40	98.10	280.30	66.20	141.90	Liu *et al.*, 2019
	10	208.92	150.19	129.53	338.67	80.19	179.20	This work
	20	230.51	188.72	170.18	389.83	69.63	199.88	
	30	280.53	241.47	210.76	432.95	68.95	226.94	
	40	328.67	290.76	250.46	489.42	95.23	257.45	
	50	359.11	329.63	293.11	508.77	100.45	280.54	

Fig 9 represents the variation of the elastics C_{ij}, the elastic modulus and the Born's criteria under the effect of pressure of $MgBi_2O_6$. We evidently detect a linear dependence in all curves of elastic constants and bulk modulus of $MgBi_2O_6$ in the considered range of pressure while C_{44} varies little under the pressure effect.

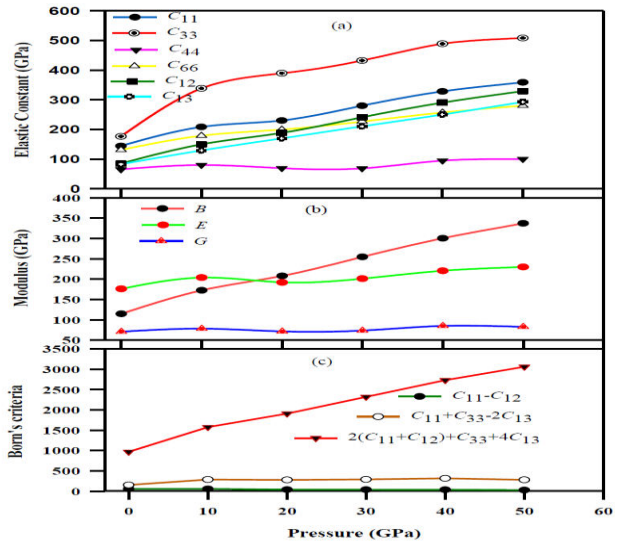

Fig 9: The calculated pressure dependence of (a) elastic constants, C_{ij}, (b) elastic modulus and (c) Born's criteria of $MgBi_2O_6$ structure.

Furthermore, C_{44} rises firstly and then decreases with pressure. The outcome is consistent with other hypothetical inquiry on a tetragonal crystal system (Benmakhlouf and Bentabet, 2015; Zhai *et al.*, 2012). The linear response of the elastic constants with pressure fulfills the Born's stability criteria (**Fig 9c**) and confirms the stability nature of $MgBi_2O_6$ up to 50 GPa. Consequently, the bulk modulus, shear modulus and Young's modulus definitely shows an increasing tendency as pressure increases (**Fig 9b**) (Zheng *et al.*, 2015).

For estimating the mechanical features of any material the most significant parameters such as the bulk modulus, shear modulus, Young's modulus, anisotropy factor, poisson's ratio of $MgBi_2O_6$ are determined through the Voigt-Reuss-Hill approximations from the investigated elastic constants C_{ij}. Depend upon the Voigt-Reuss-Hill approximations; the bulk modulus B_V and shear modulus G_V for tetragonal structure are given as:

$$B_V = \frac{2C_{11} + 2C_{12} + C_{33} + 4C_{13}}{9} \quad (2)$$

$$B_R = \frac{C^2}{M} \quad (3)$$

$$G_V = \frac{M + 3C_{11} - 3C_{12} + 12C_{44} + 6C_{66}}{30} \quad (4)$$

$$G_R = \frac{15}{\left[\frac{18B_V}{C^2} + \frac{6}{(C_{11} - C_{12})} + \frac{6}{C_{44}} + \frac{3}{C_{66}}\right]} \quad (5)$$

Where,

$M = C_{11} + C_{12} + 2C_{33} - 4C_{13}$

And $C^2 = (C_{11} + C_{12})C_{33} - 2C_{13}^2$

According to Hill the average value of B and G is given by,

$$B = \frac{1}{2}(B_R + B_v) \quad (6)$$

$$G = \frac{1}{2}(G_v + G_R) \quad (7)$$

Now to find out the values of Young's modulus (E) and Poisson's ratio (v) we have used the following relations,

$$E = \frac{9GB}{3B + G} \quad (8)$$

$$v = \frac{3B - 2G}{2(3B + G)} \quad (9)$$

The Universal anisotropic factor of a material can be calculated by the following equation Ranganathan and Ostoja-Starzewski, 2008,

$$A^U = \frac{5G_V}{G_R} + \frac{B_V}{B_R} - 6 \quad (10)$$

The calculated polycrystalline elastic constants at different pressures of $MgBi_2O_6$ by using the Eq. 2 to Eq. 10 are charted in **Table 4**. The ratio of bulk to shear modulus B/G is a sign of ductile and brittle manner of any material. The bulk modulus B indicates the resistance to volume changes via applied pressure, whereas the shear modulus G denotes the resistance to plastic deformation. The high value of B/G ratio ensures the ductility, whereas a low value corresponds to brittle manner. If $B/G > 1.75$, the material will behaves ductile manner; or else, the material will behaves brittle activities. From the value of B/G as shown in **Table 4**, we can say that this material has some toughness at ambient condition. The nature of B/G with pressure in $MgBi_2O_6$ is depicted in **Fig 10(c)**. It has been seen that when pressure increases from 0 to 50 GPa, the value of B/G changes from 1.81 to 4.07. It indicates that the compound $MgBi_2O_6$ is strongly prone to ductility at high pressure. Another recognized parameter is the Poisson's ratio, v which is used to separate the brittle solids from the ductile once proposed by Frantsevich *et al.* (1983). The larger value of Poisson's ratio ($v > 0.26$) indicates ductile manner and the compound will be brittle when the value of Poisson's ratio is ($v < 0.26$).

According to the value of ν as evident from **Table 4** this material shows ductile behavior which consistent with the result of Pugh's criteria B/G. Our results are very similar to the previous study (Liu *et al.*, 2019). **Fig 10(b)** also ensures that $MgBi_2O_6$ has little bit ductile manner at zero pressure and is strongly prone to higher ductility with increasing pressure.

Table 4: The calculated bulk modulus B (GPa), shear modulus G (GPa), Young's modulus E (GPa), B/G values, Poisson's ratio v and anisotropy factor A^U of $MgBi_2O_6$ compound at 0 to 50 GPa pressure.

Compound	Pressure (GPa)	B	G	E	B/G	v	A^U	Ref.
$MgBi_2O_6$	0	116.90	65.80	166.20	1.81	0.27	1.41	This work
		137.70	76.2	193.00	1.81	0.27	-	Liu *et al.*, 2019
	10	172.45	78.22	203.84	2.20	0.30	1.99	This work
	20	207.86	71.34	192.05	2.91	0.35	3.40	
	30	254.75	73.53	201.23	3.46	0.37	4.13	
	40	300.00	80.07	220.58	3.75	0.38	4.97	
	50	337.23	82.84	229.91	4.07	0.39	7.04	

It is well recognized that elastic anisotropy associates with anisotropic plastic deformation and activities of micro cracks in solid materials. Therefore it is very essential to determine the elastic anisotropy in super hard materials due to realized these properties and expectantly find mechanisms which will develop their hardness and mechanical durability. An appropriate explanation of anisotropic manners has a significant impact in engineering discipline as well as in crystal physics. For a pure isotropic material, AU is zero and for other case the material will be anisotropic. The value of A^U at 0 to 50 GPa of $MgBi_2O_6$ is shown in **Table 4** which is greater than zero and ensures that this compound shows anisotropic behavior. From **Fig 10(a)** it is observed that the value of A^U increases sharply with increasing pressure due to reason that that the elastic constants C_{11}, C_{33}, C_{66}, C_{12} and C_{13} are increased with pressure.

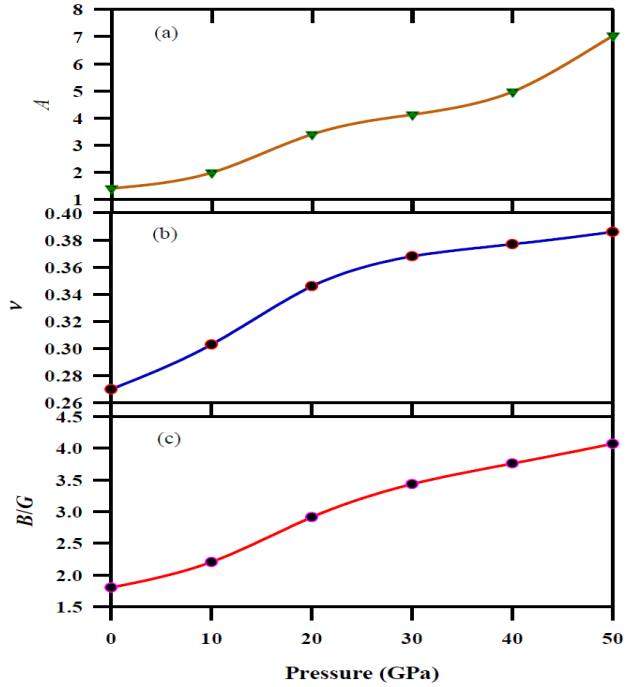

Fig 10: (a) The anisotropy factor A, (b) the Poisson's ratio v and (c) the B/G values of $MgBi_2O_6$ as a function of pressure.

3.5 Theoretical electronic and bonding properties

It is very essential to study to electronic properties of any material due to understanding the physical properties and bonding character of this material. For this reason in this study we studied the detailed electronic properties such as electronic band structure, density of states (total and partial) and the Mulliken atomic populations $MgBi_2O_6$ at zero pressure. The observed electronic band structure of this compound is depicted in **Fig 11**. A clear separation between the valence band and conduction band is observed from **Fig 11** which ensures the semiconducting behavior of $MgBi_2O_6$. This characteristic is also observed from the resistivity analysis shown in **Fig 6(a)**. The investigated electronic band gap of $MgBi_2O_6$ is about 0.121 eV which is differs from the experimental value of 1.6 eV (Mizoguchi *et al.*, 2003). This happened because DFT based calculations skip the electron's excitation effects and therefore underrate the electronic band gap (Naefa and Rahman, 2020).

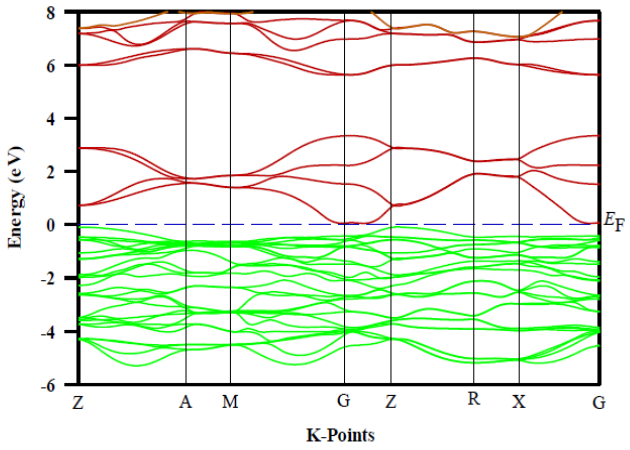

Fig 11: Electronic band structure of $MgBi_2O_6$ along high symmetry direction in the Brillouin zones.

The calculated partial and total density of states of tetragonal $MgBi_2O_6$ is exposed in **Fig 12**. The valance bands are located from -20 eV to the Fermi level and mostly created from Mg-2p, Bi-6s, O-2s and O-2p states. The conduction bands are located from 0 to 10 eV and chiefly created from Bi-6p states. However, near the Fermi level O-2p orbital contributes the most, which are the general features of oxide semiconducting materials. From **Table 5** we have seen the total density of states of this material is 3.32 states/eV, where the contribution of O-2p states is dominated. In order to understand the chemical bonding nature in compound $MgBi_2O_6$ we have studied the Mulliken atomic populations which are listed in **Table 6**. A low value of the bond population refers to the ionic behavior (For perfect ionic bond the value of the bond population is zero) whereas a high value indicates increase of covalency level (Segall *et al.*, 2003). The calculated bond populations of $MgBi_2O_6$ are shown in **Table 6**. From **Table 6** we can see that Mg and Bi atoms carry the positive charges on the other hand O atoms carry the negative charges indicating the transfer of charge from Mg and Bi to O atoms.

Table 5: Mulliken atomic populations of semiconductor $MgBi_2O_6$.

Compound	Species	s	p	Total	Charge	Bond	Population	Length (Å)
$MgBi_2O_6$	O	1.92	4.96	6.88	-0.88	O-Mg	-0.61	2.12
	O	1.92	5.01	6.93	-0.93	O-Bi	0.32	2.12
	Mg	0.36	6.13	6.49	1.51	O-Bi	0.36	2.14
	Bi	1.37	1.65	3.02	1.98	O-O	-0.12	2.72

Table 6: Total and partial density of states of $MgBi_2O_6$.

Compound	Pressure (GPa)	Partial density of states (PDOS) (electrons/eV)						Total DOS (states/eV)
$MgBi_2O_6$	0	Mg-3s	Mg-2p	Bi-6s	Bi-6p	O-2s	O-2p	3.32
		0.008	0.019	0.033	0.033	0.00	3.225	

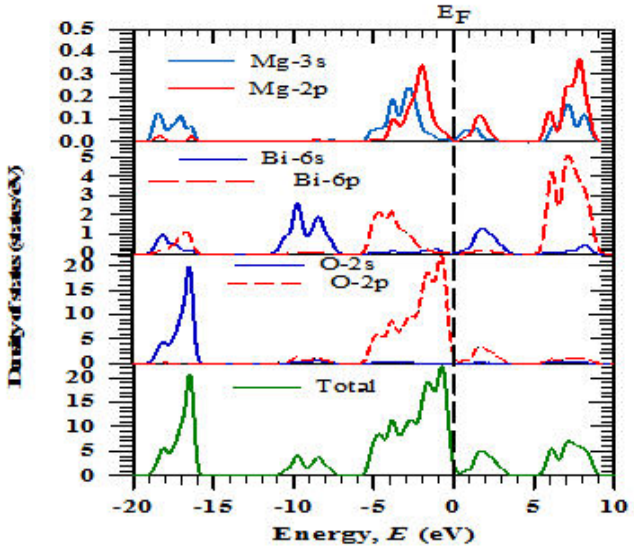

Fig 12: The total and partial density of states of $MgBi_2O_6$.

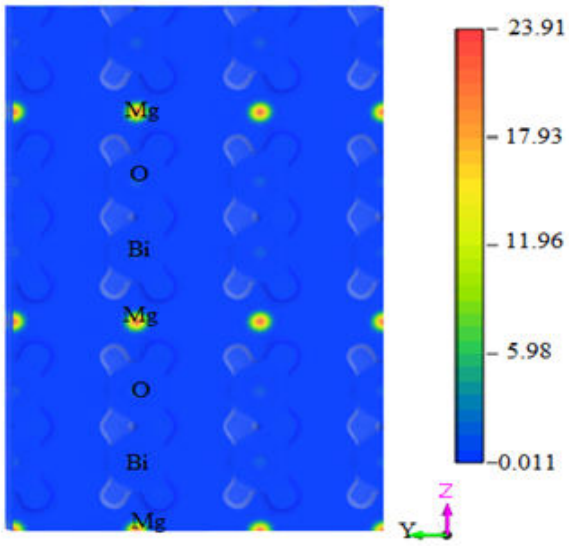

Fig 13: Total charge density map of $MgBi_2O_6$ in XYZ plane.

From Table 6 it is obvious that bond populations of bonds O-Mg and O-O are less than zero indicating the existence of ionic bond in $MgBi_2O_6$. On the other hand bond population of bonds O-Bi is greater than zero indicating the existence of covalent bond in this compound. To get comprehensible concept about the bonding features the total charge density map of $MgBi_2O_6$ is depicted in **Fig 13**. A covalent characteristic is observed in O-Bi bond due to the overlapping of charge distribution between the nearest O and Bi atoms. No overlapping of charge distribution is observed in O-Mg and O-O bonds ensure the ionic character of these bonds.

3.6 Theoretical Optical Properties

For understanding the optical properties of $MgBi_2O_6$ we studied the dielectric function, refractive index, loss function, absorption, conductivity and reflectivity by using the GGA and PBE approximations. Dielectric constants are calculated using the frequency dependent dielectric function $\varepsilon(\omega) = \varepsilon_1(\omega) + i\varepsilon_2(\omega)$, which is strongly consistent to the electronic structure. The imaginary part $\varepsilon_2(\omega)$ of this function is calculated through the following equation (Materials Studio CASTEP Manual © Accelrys, 2011):

$$\varepsilon_2(\omega) = \frac{2e^2\pi}{\Omega\varepsilon_0}\sum_{k,v,c}\left|\left\langle\psi_k^c\left|\hat{u}\cdot\vec{r}\right|\psi_k^v\right\rangle\right|^2\delta(E_k^c - E_k^v - E) \quad (11)$$

Here ω is the light frequency, e denotes the electronic charge, $\hat{u}$ denotes the vector which defining the polarization of the incident electric field, ψ_k^c and ψ_k^v are the conduction band and

valence band wave functions at k consecutively. The real part is determined via the Kramers-Kronig transforms. All the other functions are derived by Eqs., (Materials Studio CASTEP Manual © Accelrys, 2011).

The dielectric function of $MgBi_2O_6$ is shown in **Fig 14(a)** with photon energy up to 30 eV along [100] direction. From this figure it has been obvious that the static dielectric function of $MgBi_2O_6$ at 0 eV is found to be 9 eV which is contradict to the value 4.1 found by Lin Liu *et al.* (2019). The decrease of real part of the dielectric function with the increase of photon is due to the reasons that when the photon energy reaches to 0.121 eV which is the band width of this phase, the valence band electrons start to excite and move to conduction bands. Hence the carrier concentration is increases, the degree of polarization reduces and consequently the real part of the dielectric function decreases (Liu *et al.*, 2019). The non-zero region of the imaginary part indicates the happening of light absorption of this material. The imaginary part comes to zero at about 13 eV indicating that this material would be transparent after this energy range. Refractive index is an important optical function which explains the nature of electromagnetic wave through a visual medium. From **Fig 14(b)** it is obvious that the refractive index is high in the infrared and visible regions and slowly decreases in the ultraviolet region demonstrating that $MgBi_2O_6$ has strong refractive effect in the infrared and visible regions.

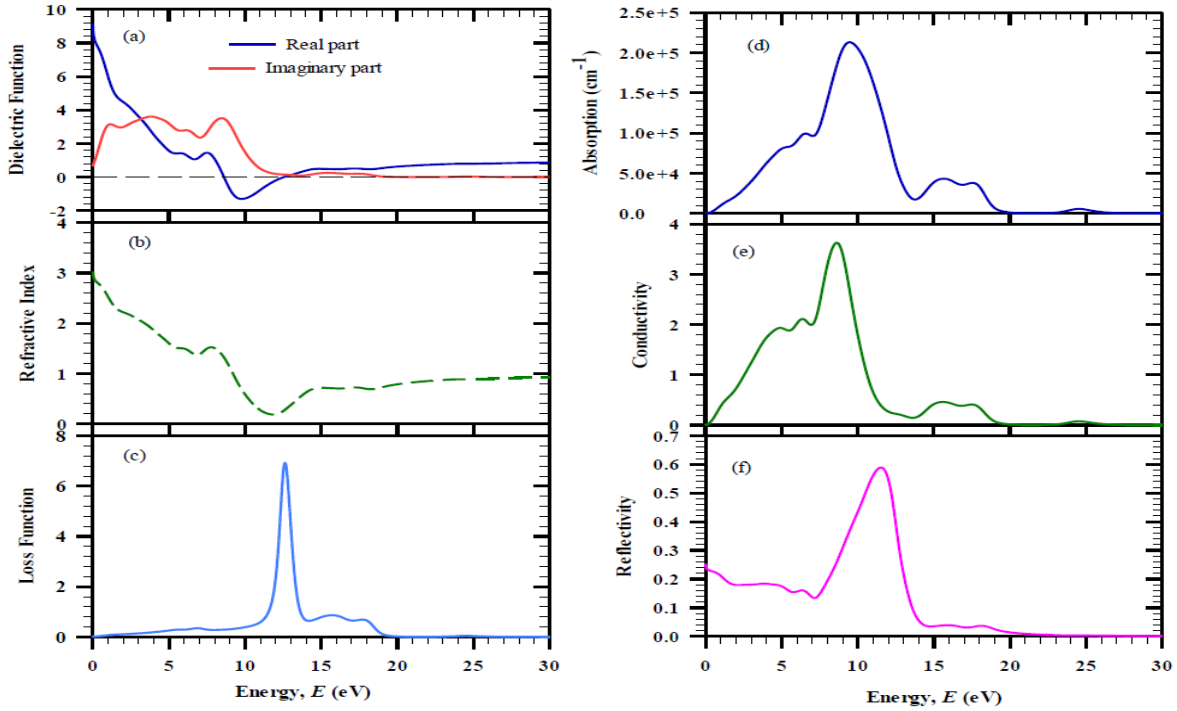

Fig 14: The investigated optical functions of $MgBi_2O_6$: (a) conductivity, (b) absorption, (c) loss function, (d) dielectric function, (e) refractive index, and (f) reflectivity.

The loss function of fast moving electron would be used to represent the resonant frequency or bulk plasma frequency ω_P of the plasma (Xu *et al.*, 2006). From **Fig 14(c)** it can be seen that the effective bulk plasma frequency is observed at 13 eV which ensures that the characteristics of plasma frequency in $MgBi_2O_6$ are obvious. This result is well agrees with our previous study (Rahman *et al.*, 2016) and did not agree with the study of Lin Liu *et al.* (2019). Therefore $MgBi_2O_6$ shows transparent behavior when the incident photon has the energy higher than this plasma frequency. The calculated absorption spectrum of $MgBi_2O_6$ depicted in **Fig 14(d)** illustrates that the light absorption edge is stared at about 0.121 eV which is comparable with the band gap determined by PBE scheme. Only one major absorption peak is found at 9 eV in the absorption spectrum. Hence it is so interesting to notice that this material absorbs ultraviolet radiation quite efficiently. The optical conductivity of $MgBi_2O_6$ starts at about 0.14 eV (**Fig 14e**) confirming again the semiconducting nature of this phase. Since the material $MgBi_2O_6$ has high absorption in the ultraviolet region as a result maximum

conductivity is observed in this region. The reflectivity shape of $MgBi_2O_6$ is shown in **Fig 14(f)**. The high reflectivity is appeared at around 13 eV which corresponds to the energy where the conductivity falls to zero and absorption quality is good. Since $MgBi_2O_6$ shows good reflectivity in the high energy area this compound should be used as a possible shield for ultraviolet radiation.

4. CONCLUSION:

In summary, the pure single phase $MgBi_2O_6$ crystal has been effectively prepared through solid-state reaction way. The polycrystalline sample $MgBi_2O_6$ has been obtained after two times calcinations at 600 and 650 °C respectively. The powder XRD patterns reveal that the prepared sample is well crystallized and indexed to a trirutile-type tetragonal crystal structure. The large grain size of about 200-350 nm as observed from SEM images ensures the increase of efficiency of $MgBi_2O_6$, when it is used as a visible light-sensitive photocatalysts. The decrease of electrical resistivity and increase of electrical conductivity with temperature ensures the semi-conducting behavior of $MgBi_2O_6$. This behavior is also observed from the electronic band structure calculations and from dielectric constant measurement. The high dielectric constant, high capacitance, high resistance, high impedance and low ac-conductance are observed at low frequency regions and consequently reverse characteristics are found in the high frequency regions. We have also performed the DFT based calculations to study the structural configuration, mechanical, electronic and optical properties of $MgBi_2O_6$. Furthermore we have observed the pressure effect on the structural and mechanical properties of the prepared product. The geometrical optimized lattice constants are very close to our experimental values which ensure the accuracy of our present work. The lattice parameters and cell volumes are decreased with the increase of pressure. The observed band gap of about 0.121 eV near the Fermi level confirms the semiconducting nature of $MgBi_2O_6$. The existence of ionic and covalent features is observed from the Mulliken atomic population calculations. The investigated elastic constants satisfied the Born's stability criteria and ensure the mechanical stability of $MgBi_2O_6$. All the elastic constants show linear response with the external pressure in which C_{33} shows more response compared to other constants. The calculated B/G ensures a little bit ductile manner of $MgBi_2O_6$ at zero pressure but this phase is strongly prone to higher ductility at high pressure. The increased of Poisson's ratio and anisotropic factor are observed with increasing pressure. The large reflectivity in the ultraviolet site ensures that $MgBi_2O_6$ should be used as a possible coating material for ultraviolet radiation.

5. ACKNOWLEDGEMENT:

We would like to thank Department of Physics, Rajshahi University, Bangladesh, and Centre for Advanced Research in Sciences, Dhaka University, Dhaka, Bangladesh for their lab support

6. CONFLICTS OF INTEREST:

The authors declared that there is no conflict of interests about this article.

7. REFERENCE:

1. Amdouni, N., Zarrouk, H. and Julien, C.M. (2003). Structural and electrochemical proper-ties of $LiCoO_2$ and $LiAlyCo1\text{-}yO_2$ (y=0.1 and 0.2) oxides: A comparative study of electrodes prepared by the citrate precursor route. *Ionics*, **9**(1-2), pp.47-55.
2. Benmakhlouf, A. and Bentabet, A. (2015). First Principles Study of Structural and Elastic Properties of $BaWO_4$ Scheelite Phase Structure under Pressure. *Elastic*, **4**(3.50), pp.5-00.
3. Chen, C., Ma, W. and Zhao, J. (2010). Semiconductor-mediated photodegradation of pollutants under visible-light irradiation. *Chemical Society Reviews*, **39**(11), pp. 4206-4219. https://doi.org/10.1039/B921692H
4. Chouhan, A.S., Athresh, E., Ranjan, R., Raghavan, S. and Avasthi, S. (2018). Ba-BiO_3: A potential absorber for all-oxide photovoltaics. *Materials Letters*, **210**, 218-222. https://doi.org/10.1016/j.matlet.2017.09.038
5. Clark, S.J., Segall, M.D., Pickard, C.J., Hasnip, P.J., Probert, M.I., Refson, K. and Payne, M.C. (2005). First principles methods using CASTEP. *Zeitschrift für Kristallographie-Crystalline Materials*, **220**(5-6), pp.567-570. https://doi.org/10.1524/zkri.220.5.567.65075
6. Fairooz, N.Y. and Imran, A.R. (2013). Wet commixing synthesis, physical properties

and photocatalytical activity of nickel oxide chromite spinel. *J Appl Chem*, **2**, pp.129-36.

7. Fujishima, A. and Honda, K. (1972). Electrochemical photolysis of water at a semiconductor electrode. *Nature*, **238**(5358), pp.37-38. https://www.nature.com/articles/238037a0
8. Fu, H., Pan, C., Yao, W. and Zhu, Y. (2005). Visible-light-induced degradation of rhodamine B by nanosized Bi2WO6. *The J. of Physical Chemistry B*, **109**(47), pp.22432-22439. https://doi.org/10.1021/jp052995j
9. Gao, X., Ruiz, P., Xin, Q., Guo, X. and Delmon, B. (1994). Preparation and characterization of three pure magnesium vanadate phases as catalysts for selective oxidation of propane to propene. *Catalysis letters*, **23**(3-4), pp.321-337. https://link.springer.com/article/10.1007/BF00811367
10. Gong, J., Lee, C.S., Kim, E.J., Kim, J.H., Lee, W. and Chang, Y.S. (2017). Self-generation of reactive oxygen species on crystalline $AgBiO_3$ for the oxidative remediation of organic pollutants. *ACS applied materials & interfaces*, **9**(34), 28426-28432. https://doi.org/10.1021/acsami.7b06772
11. Hao, Y., Lai, Q., Xu, Z., Liu, X. and Ji, X. (2005). Synthesis by TEA sol-gel method and electrochemical properties of $Li_4Ti_5O_{12}$ anode material for lithium-ion battery. *Solid State Ionics*, **176**(13-14), pp.1201-1206. https://doi.org/10.1016/j.ssi.2005.02.010
12. Hu, G.R., Liao, G., Peng, Z.D., Xiao, J., Zhang, X.L. and Yu, X.Y. (2004). Structure and electrochemical properties of $LiCoO_2$ synthesized by microwave heating. *J. of Central South University of Technology*, **11**(3), pp.261-264.
13. Janjua, N.K., Mumtaz, M., Yaqub, A., Sabahat, S. and Mujtaba, A. (2014). Electrocatalytic activity of $LiNiPO_4$ and the copper doped analogues towards oxygen reduction. *The Nucleus*, **51**, pp.109-115.
14. Jiang, X. and Wang, T. (2007). Influence of preparation method on morphology and photocatalysis activity of nanostructured TiO_2. *Environmental science & technology*, **41**(12), pp.4441-4446. https://doi.org/10.1021/es070106v
15. Julien, C.M., Massot, M. and Poinsignon, C., 2004. Lattice vibrations of manganese oxides: Part I. Periodic structures. *Spectrochimica Acta Part A: Molecular and Biomolecular Spectroscopy*, **60**(3), 689-700. https://doi.org/10.1016/S1386-1425(03)00279-8
16. Kako, T., Zou, Z., Katagiri, M. and Ye, J. (2007). Decomposition of organic compounds over $NaBiO_3$ under visible light irradiation. *Chemistry of materials*, **19**(2), 198-202. https://doi.org/10.1021/cm0611284
17. Kang, J., Lee, E.C. and Chang, K.J. (2003). First-principles study of the structural phase transformation of hafnia under pressure. *Physical Review B*, **68**(5), p. 054106. https://doi.org/10.1103/PhysRevB.68.054106
18. Khatun, F., Gafur, M.A., Ali, M.S., Islam, M.S. and Sarker, M.A.R. (2014). Impact of lithium composition on structural, electronic and optical properties of lithium cobaltite prepared by solid-state reaction. *Journal of Scientific Research*, **6**(2), pp.217-231. https://doi.org/10.3329/jsr.v6i2.17900
19. Kim, B., Kim, B.H., Kim, K., Choi, H.C., Park, S.Y., and Min, B.I. (2012). Unusual magnetic properties induced by local structure in a quasi-one-dimensional Ising chain system: α-CoV_2O_6. *Physical Review B*, **85**(22), p. 220407.
20. Kudo, A. and Miseki, Y. (2009). Heterogeneous photocatalyst materials for water splitting. *Chemical Society Reviews*, **38**(1), 253-278. https://doi.org/10.1039/B800489G
21. Kudo, A., Omori, K. and Kato, H. (1999). A novel aqueous process for preparation of crystal form-controlled and highly crystalline BiVO4 powder from layered vanadates at room temperature and its photocatalytic and photophysical properties. *J. of the American Chemical Society*, **121**(49), pp.11459-11467. https://doi.org/10.1021/ja992541y
22. Kumada, N., Takahashi, N., Kinomura, N. and Sleight, A.W. (1997). Preparation of ABi_2O_6 (A= Mg, Zn) with the trirutile-type structure. *Materials research bulletin*, **32**(8), pp.1003-1008. https://doi.org/10.1016/S0025-5408(97)00071-8
23. Linic, S., Christopher, P. and Ingram, D.B. (2011). Plasmonic-metal nanostructures for efficient conversion of solar to chemical

energy. *Nature materials*, **10**(12), 911-921. https://www.nature.com/articles/nmat3151

24. Liu, L., Wang, D., Zhong, Y. and Hu, C. (2019). Electronic, Optical, Mechanical and Lattice Dynamical Properties of MgBi2O6: A First-Principles Study. *Applied Sciences*, **9**(7), p.1267. https://doi.org/10.3390/app9071267
25. Long, M., Cai, W., Cai, J., Zhou, B., Chai, X. and Wu, Y. (2006). Efficient photo-catalytic degradation of phenol over Co3O4/BiVO4 composite under visible light irradiation. *The J. of Physical Chemistry B*, **110**(41), pp.20211-20216. https://doi.org/10.1021/jp063441z
26. Materials Studio CASTEP Manual© Accelrys, 2010. http://www.tcm.phy.cam.ac.uk/castep/documentation/WebHelp/CASTEP.html
27. Matsuda, S. and Hatano, H. (2005). Photo-catalytic removal of NOx in a circulating fluidized bed system. *Powder technology*, **151**(1-3), pp.61-67. https://doi.org/10.1016/j.powtec.2004.11.031
28. Meng, X. and Zhang, Z. (2016). Bismuth-based photocatalytic semiconductors: introduction, challenges and possible approaches. *J. of Molecular Catalysis A: Chemical*, **423**, pp.533-549. https://doi.org/10.1016/J.MOLCATA.2016.07.030
29. Mizoguchi, H., Bhuvanesh, N.S. and Woodward, P.M. (2003). Optical and electrical properties of the wide gap, n-type semiconductors: $ZnBi_2O_6$ and $MgBi_2O_6$. *Chemical Communic.*, **9**, pp.1084-1085. https://doi.org/10.1039/b300635b
30. Mostari F, Rahman MA, and Khatun R. (2020). First principles study on the structural, elastic, electronic and optical properties of cubic 'half-Heusler' alloy RuVAs under pressure, *Int. J. Mat. Math. Sci*., **2**(4), 51-63. https://doi.org/10.34104/ijmms.020.051063
31. Naefa MJ, and Rahman MA. (2020). First principles study of structural, elastic, electronic and optical features of the non-centrosymmetric superconductors SrMGe3 (Where M= Ir, Pt, and Pd), *Int. J. Mat. Math. Sci*., **2**(2), 16-28. https://doi.org/10.34104/ijmms.020.016028
32. Perdew, J.P., Burke, K. and Ernzerhof, M. (1996). Generalized gradient approximation made simple. *Physical review letters*, **77**(18), p.3865. https://doi.org/10.1103/PhysRevLett.77.3865
33. Rahman, M.A., Rahman, M.A., Chowdhury, U.K., Bhuiyan, M.T.H., Ali, M.L. and Sarker, M.A.R. (2016). First principles investigation of structural, elastic, electronic and optical properties of ABi_2O_6 (A=Mg, Zn) with trirutile-type structure. *Cogent Physics*, **3**(1), p.1257414. https://doi.org/10.1080/23311940.2016.1257414
34. Rahman, M.A., Rahaman, M.Z. and Rahman, M.A. (2016). The structural, elastic, electronic and optical properties of MgCu under pressure: A first-principles study. *International Journal of Modern Physics B*, **30**(27), p.1650199. https://doi.org/10.1142/S021797921650199X
35. Ranganathan, S.I. and Ostoja-Starzewski, M. (2008). Universal elastic anisotropy index. *Physical Review Letters*, **101**(5), p. 055504. https://doi.org/10.1103/PhysRevLett.101.055504
36. Sarkar, K. and Mukherjee, S. (2016). Synthesis, characterization and property evaluation of single phase $MgNb_2O_6$ by chemical route. *Journal of The Australian Ceramic Society*, **52**(2), pp.32-40.
37. Segall, M.D., Shah, R., Pickard, C.J. and Payne, M.C. (1996). Population analysis of plane-wave electronic structure calculations of bulk materials. *Physical Review B*, **54**(23), p.16317. https://doi.org/10.1103/PhysRevB.54.16317
38. Song, J.M., Lin, Y.Z., Yao, H.B., Fan, F.J., Li, X.G. and Yu, S.H. (2009). Super long β-$AgVO_3$ nanoribbons: high-yield synthesis by a pyridine-assisted solution approach, their stability, electrical and electrochemical properties. *ACS nano*, **3**(3), pp. 653-660. https://doi.org/10.1021/nn800813s
39. Takei, T., Haramoto, R., Dong, Q., Kumada, N., Kameshima, Y. and Miyake, M. (2011). Photocatalytic activities of various penta-valent bismuthates under visible light irradiation. *J. of Solid State Chemistry*, **184**(8), pp.2017-2022. https://doi.org/10.1016/j.jssc.2011.06.004
40. Tang, Y., Zhou, J., Liu, J., Liu, L.X., Liang, S.Q. and Li, Y. (2013). Facile synthesis of

cobalt vanadium oxides and their applications in lithium batteries. *Mater. Lett*, **8**, pp.1138-1145. http://www.electrochemsci.org/papers/vol8/80101138.pdf

41. Tang, J., Zou, Z. and Ye, J. (2007). Efficient photocatalysis on $BaBiO_3$ driven by visible light. *The Journal of Physical Chemistry C*, **111**(34), pp.12779-12785. https://doi.org/10.1021/jp073344l
42. Usha, V., Kalyanaraman, S., Vettumperumal, R. and Thangavel, R. (2017). A study of frequency dependent electrical and dielectric properties of NiO nanoparticles. *Physica B: Condensed Matter*, **504**, 63-68. https://doi.org/10.1016/j.physb.2016.10.011
43. Wang, J. and Zhou, Y. (2004). Dependence of elastic stiffness on electronic band structure of nanolaminate M_2AlC (M= Ti, V, Nb, and Cr) ceramics. *Physical Review B*, **69**(21), p.214111.
44. Wang, C.Y., Zhang, X., Qiu, H.B., Wang, W.K., Huang, G.X., Jiang, J. and Yu, H.Q. (2017). Photocatalytic degradation of bisphenol A by oxygen-rich and highly visible-light responsive $Bi_{12}O_{17}C_{l2}$ nanobelts. *Applied Catalysis B: Environmental*, **200**, pp.659-665. https://doi.org/10.1016/j.apcatb.2016.07.054
45. Xu, M., Wang, S., Yin, G., Li, J., Zheng, Y., Chen, L. and Jia, Y. (2006). Optical properties of cubic Ti_3N_4, Zr_3N_4, and Hf_3N_4. *Applied physics letters*, **89**(15), p.151908. https://doi.org/10.1063/1.2360937
46. Zhai, H., Li, X. and Du, J. (2012). First-principles calculations on elasticity and anisotropy of tetragonal tungsten dinitride under pressure. *Materials transactions*, **53**(7), pp.1247-1251. https://doi.org/10.2320/matertrans.M2011373
47. Zhang, C., Kou, L., He, T., Jiao, Y., Liao, T., Bottle, S. and Du, A. (2018). First principles study of trirutile magnesium bismuth oxide: Ideal bandgap for photovoltaics, strain-mediated band-inversion and semiconductor-to-semimetal transition. *Computational Materials Science*, **149**, pp.158-161.
48. Zheng, B., Zhang, M. and Luo, H.G. (2015). Pressure effect on structural, elastic, and thermodynamic properties of tetragonal B_4C_4. *AIP Advances*, **5**(3), p. 037123. https://cyberleninka.org/article/n/475053
49. Zhong, L., Hu, C., Zhu, B., Zhong, Y. and Zhou, H. (2018). Synthesis and photocatalytic properties of $MgBi_2O_6$ with Ag additions. In *IOP Conference Series: Earth and Environmental Science*, **121**, p. 022022. https://doi.org/10.1088/1755-1315/121/2/022022
50. Zou, Z., Ye, J., Sayama, K. and Arakawa, H. (2011). Direct splitting of water under visible light irradiation with an oxide semiconductor photocatalyst. In *Materials for Sustainable Energy: A Collection of Peer-Reviewed Research and Review Articles from Nature Publishing Group,* pp. 293-295. https://doi.org/10.1142/9789814317665_0044

Citation: Rahman MA, Rahman MA, and Sarker AR. (2020). Synthesis, characterization and pressure effect on structural and mechanical properties of $MgBi_2O_6$: solid-state route and DFT study, *Int. J. Mat. Math. Sci.*, **2**(5), 71-86. https://doi.org/10.34104/ijmms.020.071086